RSC Advances

PAPER

View Article Online
View Journal | View Issue

Cite this: *RSC Adv.*, 2025, **15**, 12372

Oxygen-rich carbon cloth as a lithium deposition host for stable lithium metal anodes†

Yan Wang, *[a] Chunxiao He,[a] Xiaodong Sun[b] and Xianyu Liu [c]

Li metal is known as the most ideal anode material for Li-ion batteries due to its high theoretical capacity (3860 mA h g^{-1}) and low redox potential (−3.04 V *vs.* SHE). However, the dendrite growth and volume expansion caused by inhomogeneous and loose Li deposition limit the practical application of Li metal anode. Herein, oxidized carbon cloth (OCC) modified with oxygen-containing functional groups (–COOH, –C–OH, C=O) is prepared by oxidation in a water bath environment. The polar oxygen-containing functional groups enhance the adsorption capacity of Li^+, reduce the nucleation barrier, and effectively regulate the uniform distribution of Li^+ on carbon fiber. Meanwhile, the large specific surface area of carbon fiber can reduce the local current density and inhibit dendrite formation. The sufficient internal space of the OCC can store the deposited Li, effectively easing the volume expansion. As such, the OCC||Li half-cells exhibit a high coulombic efficiency (98.2%) after 250 cycles at 1 mA cm^{-2}. Besides, the OCC||$LiFePO_4$ full cell capacity is 117 mA h g^{-1} after 300 cycles at 1C. The experimental results show that the OCC prepared by a simple and efficient oxidation method plays a positive role in exploring high energy density Li metal batteries.

Received 2nd March 2025
Accepted 11th April 2025

DOI: 10.1039/d5ra01479d

rsc.li/rsc-advances

1. Introduction

To realise the future demand for high-performance energy storage systems, the development of safe and high energy density Li-ion batteries has become a priority.[1] Among the various anode materials for Li-ion batteries (carbon-based materials,[2] metals,[3] metal oxides,[4] *etc.*), Li-metal anode is known as the "Holy Grail" anode due to its theoretical capacity of up to 3860 mA h g^{-1} and low redox potential of −3.04 V (relative to standard hydrogen electrode).[5] In parallel, the Li–sulfur batteries, Li–oxygen batteries and other new batteries composed of Li metal anode have the advantage of high energy density.[6] However, Li dendrite growth and volume expansion issues have limited the development of Li metal anode. According to the space charge model, the space charge region is formed on the negative surface of Li metal due to the reciprocal migration of cations and ions during the discharge process, and the strong negative electric field induces the uneven deposition of Li ion to form Li dendrites, which can puncture the separator and cause a short circuit.[7] In addition, the hostless nature of the Li metal anode leads to loosely deposited Li, causing rupture of the SEI membrane.[8] The reconfiguration of the SEI film increases its thickness and consumes Li metal, leading to increased impedance and reduced Coulomb efficiency.[9]

To address the above problems, several strategies have been proposed: (1) *in situ* generation of SEI membranes (through modification of the electrolyte or chemical reaction with Li) or construction of artificial SEI membranes;[10–12] (2) preparation of solid-state electrolytes;[13,14] and (3) introduction of three-dimensional framework structures (including metal-based frameworks,[15] carbon-based frameworks,[16] and polymer frameworks[17]). Among them, the 3D frame structure can solve the problem of Li dendrite growth and volume expansion simultaneously.[18] Compared with metal frames (Cu foam,[19] Ni foam,[20] *etc.*) and polymer frames (PVDF),[21] carbon frames (carbon nanotubes,[22] carbon cloth[23,24] and porous carbon,[25] *etc.*) have the advantages of low mass density and high conductivity, which is the best choice for the development of high energy density Li metal batteries. At present, researchers have solved the problem of poor Li affinity of carbon materials by modifying them with lithophilic components (Sn,[26] Ag,[27] ZnO,[28] MnO_2,[29] NiO and CoF_2,[30] *etc.*). However, the alloying of metals with Li and the conversion process of metal oxides/metal sulphides with Li cause volume expansion and partially irreversible reactions, resulting in reduced Coulomb efficiency and increased internal resistance of the battery.[31] In contrast, the introduction of lithophilic polar functional groups on the surface of the carbon cloth (CC) by means of low-cost and efficient acid oxidation can avoid the above problems and further improve the energy density of the battery.[32,33]

[a]*College of Petroleum and Chemical Engineering, Longdong University, Qingyang, 74500, China. E-mail: wangyan_19881108@sina.com*

[b]*Institute of Materials and Technology, Dalian Maritime University, Dalian, 116026, China*

[c]*Bailie School of Petroleum Engineering, Lanzhou City University, Lanzhou 730070, China*

† Electronic supplementary information (ESI) available. See DOI: https://doi.org/10.1039/d5ra01479d

Herein, the oxidized carbon cloth (OCC) modified with polar functional groups (–COOH, –C–OH, C═O) was prepared by simple oxidation method as the host for Li deposition. The deposition/stripping behavior of Li on the OCC is studied, and the volume change and dendrite growth of composite electrode after cycling are observed. The lithophilicity of the polar functional group as the active site lowers the Li nucleation barrier and induces dense Li deposition. Meanwhile, the sufficient internal space of the OCC can accommodate the deposited Li, effectively improving the volume change during cycling. As a result, the OCC-Li symmetric cells can stably cycle for 500 h at 1 mA cm^{-2}, 1 mA h cm^{-2} with a polarization voltage of 30 mV.

2. Experimental section

2.1 Synthesis of the OCC

The OCC framework was prepared by acid oxidation method in a water bath environment. Firstly, the commercial carbon cloth (HCP331, CC) was sonicated in deionized water (lab-made) and alcohol (AR) for 30 min respectively to remove the surface impurities. The CC was then placed into a configured mixed acid solution (V H_2SO_4 : V HNO_3 = 1 : 1, AR, Xinhua Pharmaceutical Co. Ltd) and magnetically stirred for 6 h at 60 °C in a water bath environment. The oxidized OCC was washed three times with deionized water and alcohol to remove the residual acid, respectively, with a duration of 1 min for each wash. Finally, the OCC was placed in a vacuum drying oven for 12 h and then cut into circular plate with a diameter of 10 mm.

2.2 Cell assembly

Three different types of CR2032 coin cells need to be assembled in a glove box filled with argon gas, which were half cells, symmetric cells and full cells.

2.2.1 Half cells assembly. The OCC‖Li and CC‖Li half cells were assembled with OCC and CC as working electrodes, Li foil as counter electrode, Celgard 2320 as separator and DME (ethylene glycol dimethyl ether)/DOL (1,3-dioxolane) (volume ratio 1 : 1) with 1 M LiTFSI (lithium bis(trifluoromethanesulfonyl)imide) added with 5% $LiNO_3$ as electrolyte.

2.2.2 Full cells assembly. The OCC-Li‖$LiFePO_4$ cells were assembled with $LiFePO_4$ as cathode, OCC-Li as anode and 1 M $LiPF_6$ dissolved in DMC (dimethyl carbonate)/EC (vinyl carbonate) (volume ratio 1 : 1) as electrolyte, and the diaphragm was the same as above. In addition, The $LiFePO_4$ electrodes were obtained by grinding a mixture of $LiFePO_4$, super P and poly vinylidene fluoride with a mass ratio of 8 : 1 : 1 for 1 hour. The CC-Li‖$LiFePO_4$ full cells were assembled in the same way as described above.

2.2.3 Symmetric cells assembly. Firstly, the OCC electrodes were predeposited with 3 mA h cm^{-2} Li in OCC‖Li half cells. Then the half cells were disassembled to obtain the OCC-Li composite electrodes. Finally, the OCC-Li electrodes were used as both cathode and anode of the cells to assemble OCC-Li‖OCC-Li symmetric cells. The CC-Li‖CC-Li symmetric cells were assembled in the same way as described above.

2.3 Material characterization

The X-ray diffractometer (XRD, Rigaku D/MAX-3A) with D/TeX-Ultra point detector and Co-Kα (λ = 1.789 Å) was used to analyse the crystal structure of the materials. The tube current and tube voltage were 40 mA and 40 kV with a scan rate of 4°/min, respectively. The Field Emission Scanning Electron Microscopy (FESEM, SUPRA55/SAPPHIRE) was used to observe the microscopic morphology and dimensions of the material, which was coupled with an X-Max Energy Dispersive Spectrometer (EDS) to qualitatively analyse the elements of the samples. The accelerating voltage was maintained at 3 kV and 20 kV during the experiments using SEM and EDS, respectively. The Fourier Transform Infrared Spectrometer (FTIR, Spectrum 3) with EverGloTM light source (15–9600 cm^{-1}) was used to characterise functional groups and chemical bonding information in the materials. The X-ray photoelectron spectroscopy (XPS, Thermo Kalpha) with Al Kα radiation (E = 1486.6 eV) was used to test the types and chemical states of elements on the surface of materials in a vacuum ($\sim 2 \times 10^{-9}$ mbar). The degree of graphitization of carbon materials and the degree of disorder of carbon atom arrangement were characterized by Raman Spectrometer (T64000). The laser wavelength was 532 nm.

2.4 Electrochemical characterization

For CE measurement, the OCC‖Li and CC‖Li half cells were first activated for 3 cycles at 0.01–1 V at 100 μA cm^{-2} on a Land system (CHI660D). Then, 1 mA h cm^{-2} Li was deposited to the OCC and CC electrodes and stripped to 1 V under different current densities at the same cycle.

For polarization voltage and rate performance measurement, the OCC-Li‖OCC-Li and CC-Li‖CC-Li symmetric cells were studied with 1 mA h cm^{-2} at different current densities on a Land system (CHI660D). For electrochemical impedance spectroscopy (EIS) testing, the OCC-Li‖OCC-Li and CC-Li‖CC-Li symmetric cells were performed on an electrochemical workstation (CHI660D) from 0.01 to 10^5 Hz. The OCC-Li‖LFP and CC-Li‖LFP full cells were examined for long cycle and rate performance on a Land system (CHI660D) in the voltage range 2.3–4.0 V.

3. Results and discussion

The preparation process of the OCC is shown in Fig. 1. The commercial carbon cloth (CC) was placed in a beaker containing mixed acid (V H_2SO_4 : V HNO_3 = 1 : 1) and stirred in a water bath at 60 °C for 6 hours. Then the OCC was washed with deionized water (lab-made) and alcohol (AR) respectively to remove impurities and residual acids on the OCC. Finally, the OCC was dried in a vacuum drying oven.

The diagram of Li deposition on CC and OCC is provided in Fig. 2. The uneven deposition and aggregation of Li on CC results in the formation of dendrite Li due to the poor lipophilicity of CC (Fig. 2a). In contrast, the uniformly distributed oxygen-containing functional groups on the OCC surface have excellent lithiophilic, which can reduce the nucleation barrier of Li, resulting in the uniform and dense Li deposition on the

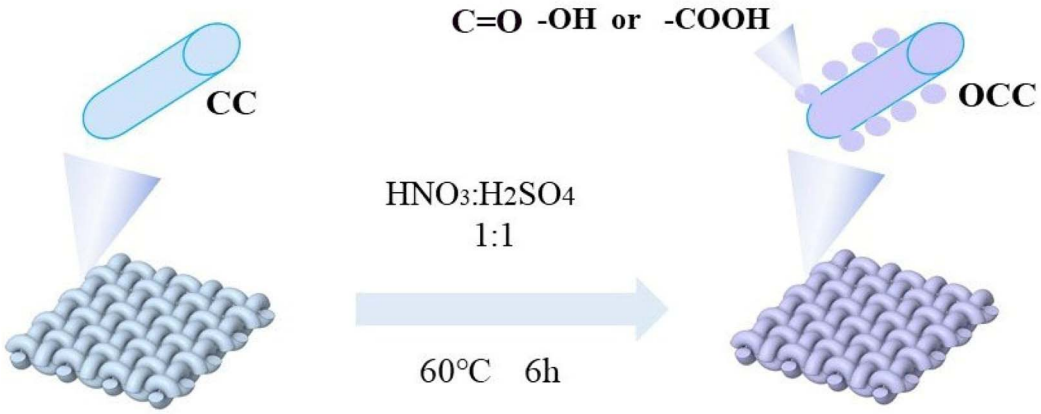

Fig. 1 Schematic diagram of the OCC preparation process.

surface of carbon fiber (Fig. 2b). Li repeated deposition and stripping on carbon fiber will not produce aggregation and shedding, which effectively inhibits the growth of Li dendrites.

The microscopic morphology of the OCC is shown in Fig. 3. As shown in Fig. 3a, the OCC is woven with carbon fiber, which has regular surface topography. The carbon fiber has a smooth surface and a diameter of about 10 μm (Fig. 3b). The element distribution map of the OCC indicates the presence of C and O elements (Fig. 3c).

The XRD pattern is provided to analyse the crystal structures of the OCC and CC (Fig. 4a). The OCC and CC diffraction peaks of conspicuous large drums located at 24.5° and 43.5° correspond to the (002) and (100) crystal planes of carbon, respectively, proving the carbon amorphous structure. As shown in Fig. 4b, the functional group information of the CC and OCC surfaces is analysed using FTIR. The absorption peaks at wave numbers of 870, 1146 and 1395 cm^{-1} in the spectrogram of the OCC correspond to the stretching vibration of the C–O bond, while the peak at 1617 cm^{-1} and 1675 cm^{-1} are caused by the stretching vibration of the C=O bonds in the carboxyl and aldehyde groups, which proves that oxygen-containing functional groups (–COOH, –C–OH, C=O) have been successfully introduced on the surface of the carbon fibre by the oxidation treatment. In contrast, the infrared spectrum of the CC has no characteristic peaks of functional groups.

The XPS test further probes the chemical bonding information on the CC and OCC surface. The XPS full spectrum of OCC proves the existence of C and O elements (Fig. S1a†). And C O atomic ratios are provided in Table S1.† However, the presence of oxygen peak in the full spectrum of CC is attributed to the adsorption of oxygen from air by CC (Fig. S1b†). In the O 1s spectrum of the OCC, the –C=O (530.6 eV), –COOH (532.1 eV) and –C–OH (533.4 eV) peaks are observed, which correspond to the FTIR test results (Fig. 4c). Tables S2 and S3† present the fitted parameters and peak positions for O 1s, respectively. In addition, the Raman spectra characterise the degree of carbon disorder using the peak intensity ratio (I_D/I_G) in the D and G bands (Fig. 4d). Here, the D band represents the degree of graphitization of carbon and G band represents the degree of disorder of carbon. The value of I_D/I_G of the OCC (1.13) is greater

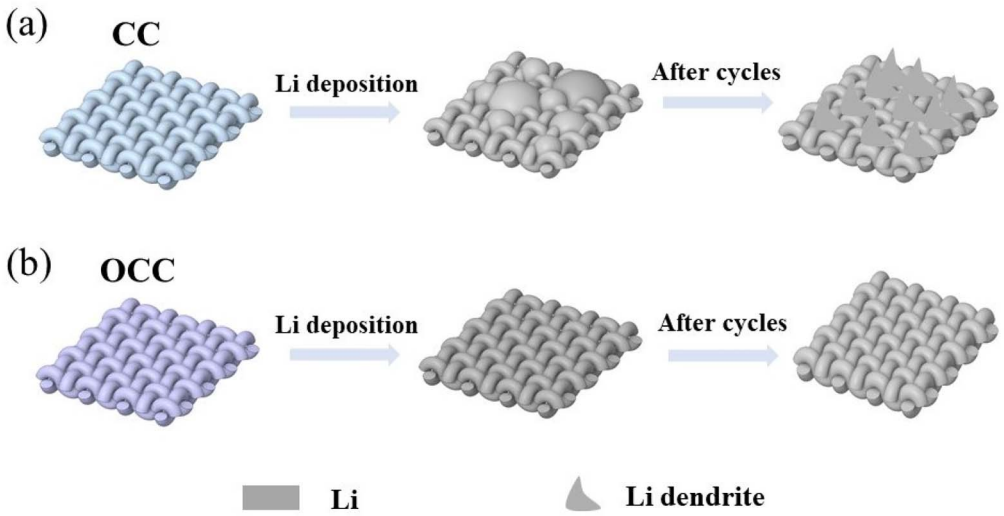

Fig. 2 The diagram of Li deposition on the (a) CC and (b) OCC.

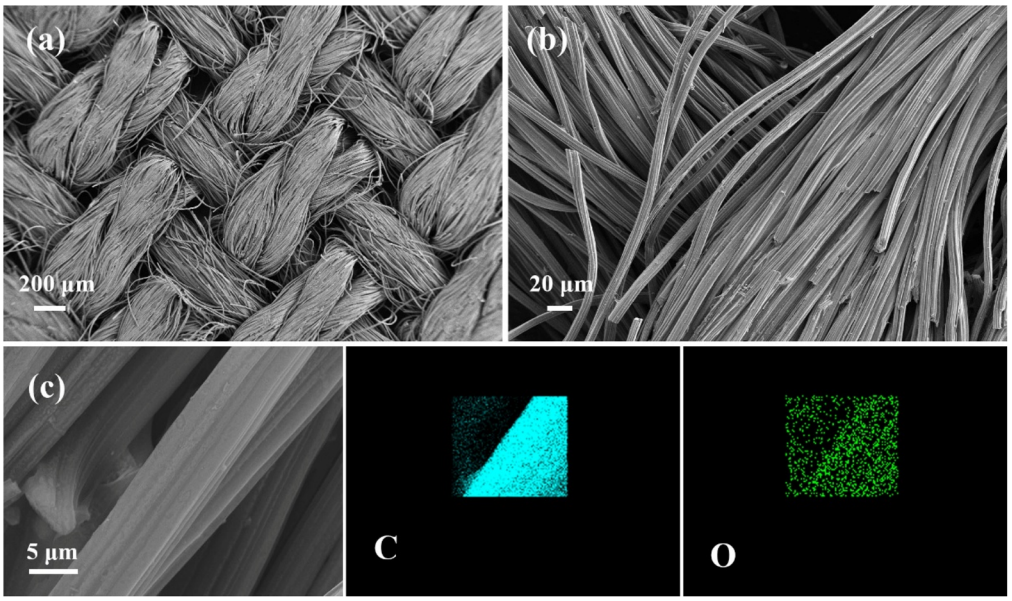

Fig. 3 (a and b) SEM images of the OCC. (c) EDS mapping images of the OCC.

than that of CC (1.00), indicating the increase of OCC defects, which indirectly proves the successful introduction of functional groups.

To investigate the Li deposition behaviour on the OCC and CC, the microscopic cross-sections of the initial OCC, CC electrodes and the OCC-Li, CC-Li composite electrodes after cycling

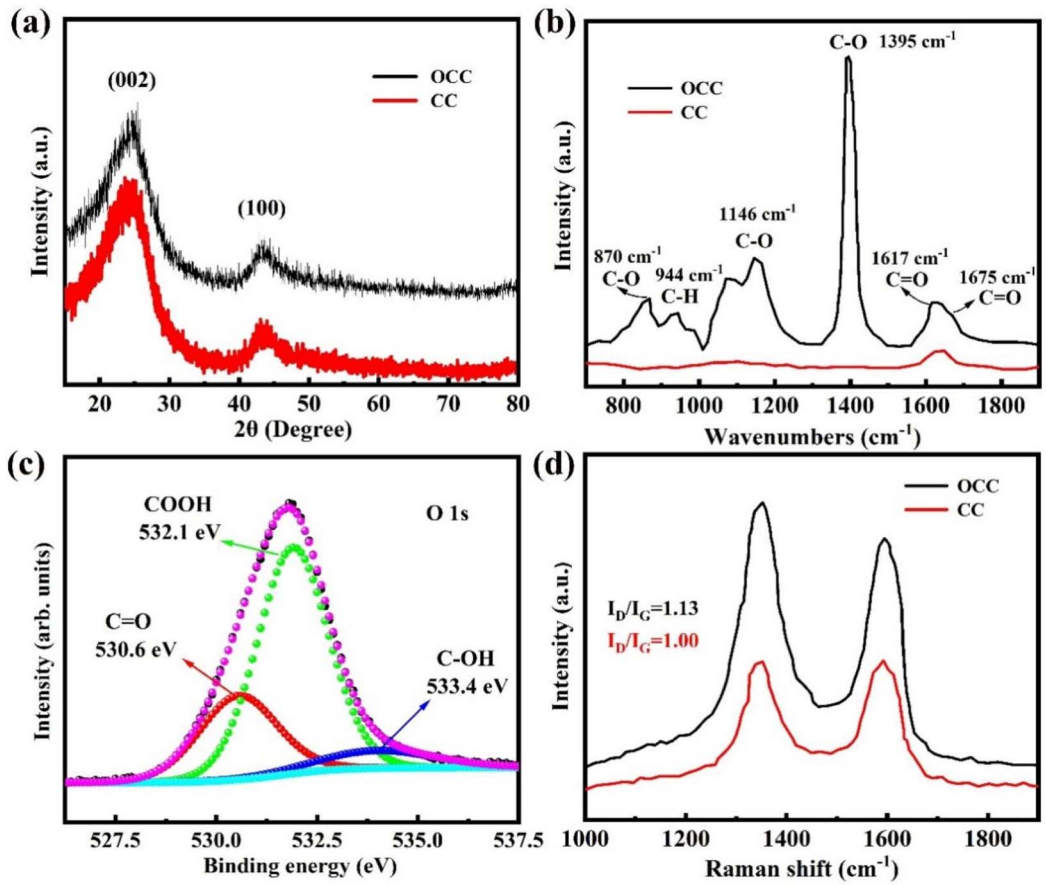

Fig. 4 (a) XRD patterns; (b) FT-IR spectra; (c) O 1s XPS spectrum; and (d) Raman spectra for the OCC.

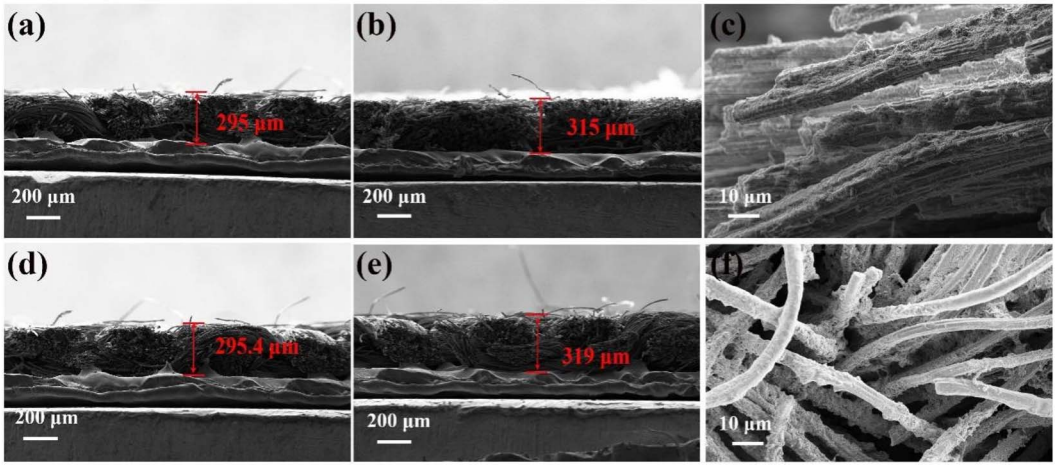

Fig. 5 Electrode microscopic cross-section morphology (a and d) original OCC and CC; (b and e) OCC-Li and CC-Li composite electrodes after 50 cycles; (c and f) magnifications of OCC-Li and CC-Li composite electrodes after 50 cycles.

are observed (Fig. 5). The cross-sectional thicknesses of the OCC and CC electrodes are 295 μm and 295 μm, respectively (Fig. 5a and d). While the cross-sectional thicknesses of the OCC-Li and CC-Li composite electrodes are increased to 315 μm and 324 μm after 50 cycles, respectively (Fig. 5b and e). In addition, the cross-section magnification of the OCC-Li and CC-Li electrodes after cycling shows that Li deposits uniformly on the OCC and accumulates on the CC (Fig. 5c and f). The thickness variation of the OCC-Li electrode section is smaller than that of CC-Li, which proves that the lithiophilic OCC induces Li deposition in the interior of the framework, effectively regulating the Li^+ distribution and alleviating the volume change.

To compare the ease of Li nucleation on the CC and OCC, the nucleation overpotentials at 1 mA cm^{-2} and 5 mA cm^{-2} are tested. The nucleation overpotential is defined as the voltage difference between the lowest voltage and the final voltage plateau in the discharge voltage, which is normally used to assess the difficulty of nucleation. As shown in Fig. 6a, when the current density is 1 mA cm^{-2}, the nucleation potential, crystal core growth potential and nucleation overpotential of Li on the OCC are 74 mV, 32 mV and 42 mV, respectively. The nuclear potential of Li on CC is 230 mV, and the voltage gradually rises to 80 mV after nucleation, with a difference of 150 mV. when the current density is 5 mA cm^{-2}, the Li nucleation potentials on the OCC and CC are 92, 337 mV, crystal core growth potentials are 27, 88 mV, and nucleation overpotentials are 65, 248 mV (Fig. S2†). The results indicate that Li has a lower nucleation barrier on the OCC and the increase of current density will increase the difficulty of nucleation.

To investigate the deposition/stripping reversibility of Li on the OCC and CC, the OCC and CC electrodes are deposited with 1 mA h cm^{-2} Li and then stripped to 1 V at different current densities. CE is defined as the ratio of stripped Li capacity to deposited Li capacity within the same cycle. When the test current density is 1 mA cm^{-2} (Fig. 6c), the initial CE of the OCC||Li is 99.5%, which is greater than that of the CC||Li (96.2%). The CE of the OCC||Li remains at 99.1% after 250 cycles, which is attributed to the uniform distribution of lithiophilic functional groups on the OCC. In contrast, the CE of CC||Li is only 70.57% after 146 cycles, indicating that dead Li is generated during the cycle. The corresponding voltage capacity curves show that the charge–discharge curves of the OCC||Li with different cycle numbers have high overlap and the charge–discharge curves of the CC||Li move to the left as the number of cycles increases (Fig. 6b and S3†). When the current density is 3 mA cm^{-2} (Fig. S4†), the CE of the OCC||Li is 97.72% after 180 stable cycles. While the CE of CC||Li dropped after 70 cycles, and the CE is only 68.54% when cycling 130 cycles. Increasing the current density to 5 mA cm^{-2} (Fig. 6d), the OCC||Li still maintain a high CE (97%) after 100 cycles, while the CC||Li fails after 30 cycles. The results illustrate that the oxygen-containing functional groups in the OCC act as Li nucleation sites to induce uniform deposition of Li on the carbon fibre surface, resulting in high reversibility and stability of Li deposition/stripping.

To explore the cyclic stability of the OCC-Li and CC-Li composite electrodes, the OCC-Li||OCC-Li and CC-Li||CC-Li cells are tested at 1 mA h cm^{-2} at different current densities. When the current density is 1 mA cm^{-2} (Fig. 7a), the OCC-Li||OCC-Li cell can stably cycle for 500 h with a polarization voltage of 15 mV. While the polarization voltage of the CC-Li||CC-Li cell gradually increases after cycling for 100 h, which is greater than the initial 52 mV. At 3 mA cm^{-2} (Fig. S5†), the OCC-Li||OCC-Li cell maintains a low polarization voltage (27 mV) for a stable cycle of 300 h. However, the voltage of CC-Li||CC-Li cell fluctuates after cycling for 50 h. Increasing the current density to 5 mA cm^{-2} (Fig. 7b), the polarization voltage of the OCC-Li||OCC-Li cell increases (50 mV). In contrast, the CC-Li||CC-Li symmetrical cell shows obvious voltage polarization after cycling at a stable polarization voltage (138 mV) for 30 h. The results show that the OCC-Li electrode has strong interfacial stability and dendrite tolerance, while the CC-Li electrode polarization increases due to the uneven deposition of Li and the occurrence of side reactions during the cycle.

Meanwhile, the rate performance of the symmetric cells can further understand the voltage polarization at different current

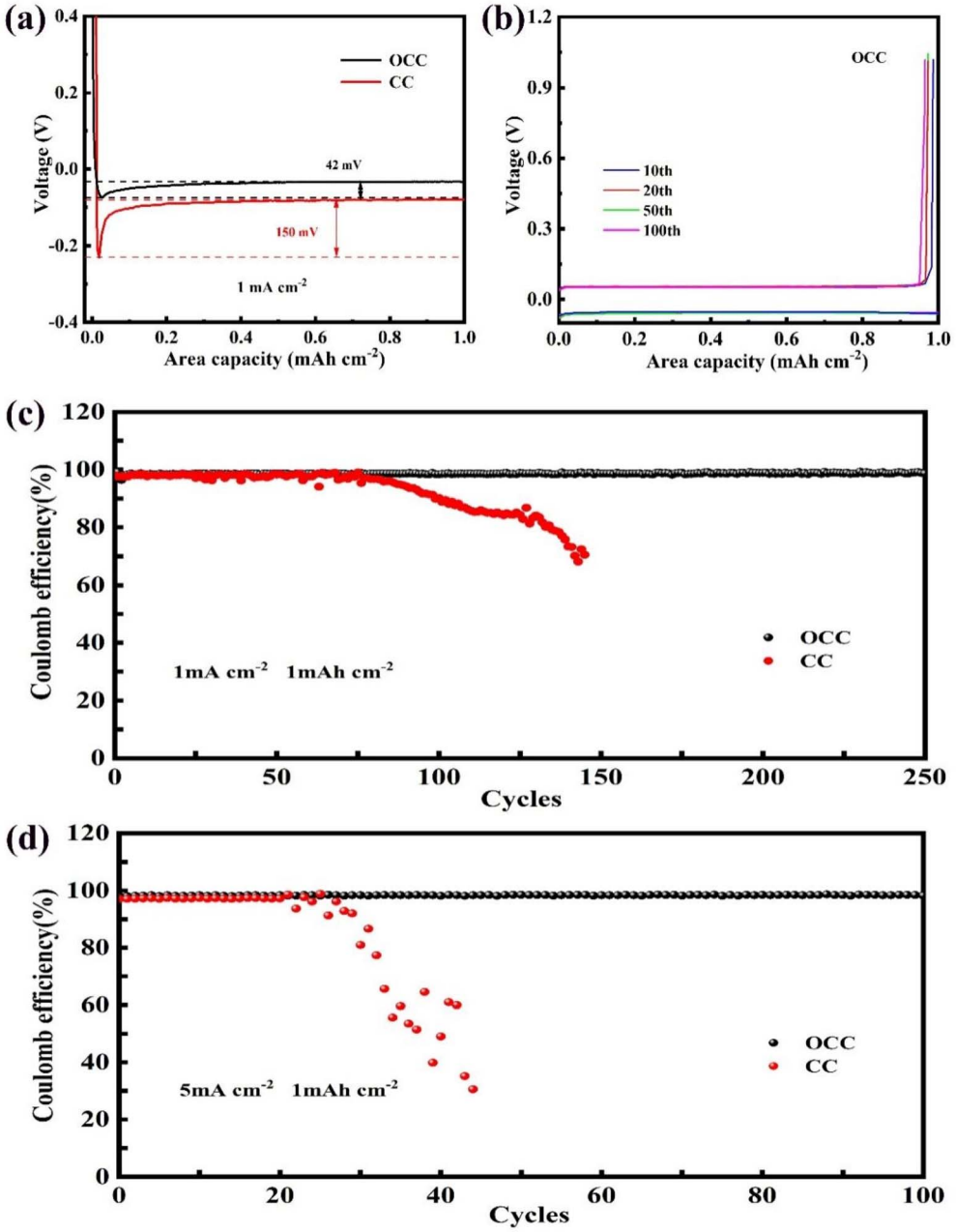

Fig. 6 (a) Nucleation overpotentials of Li on the OCC and CC at 1 mA cm^{-2}. (b) Voltage–capacity curves of the OCC||Li at different cycles. (c and d) CE of the OCC||Li and CC||Li cells at 1 mA cm^{-2} and 5 mA cm^{-2}.

densities (Fig. 7c). With the variation of current density (0.5, 1, 2, 5, and 0.5 mA cm^{-2}), the polarisation voltage (15, 23, 42, 73, 14 mV) of the OCC-Li||OCC-Li cell always remains stable, while the CC-Li||CC-Li cell exhibits significant voltage fluctuation (28, 52, 71, 270, 14 mV) at 5 mA cm^{-2}, which proves the excellent rate performance of the OCC-Li. To investigate the kinetic processes in the OCC-Li||OCC-Li and CC-Li||CC-Li cells, the EIS is tested. The R_{ct} (semicircle in the high frequency region) represents the charge transfer resistance at the electrode/electrolyte interface, while the Z_w (the slope of the low frequency region) represents the diffusion resistance of Li^+ in the electrolyte. As shown in Fig. 7d, the OCC-Li has a smaller R_{ct}, which is attributed to the more stable electrode interface of the OCC-Li, while the larger slope of the OCC-Li in the low frequency region proves that the Li^+ has stronger diffusion kinetics. In addition, the EIS of symmetrical cells after cycling are tested in Fig. S6.† The increased R_{ct} of CC is due to the repeated reconfiguration of SEI.

To explore more intuitively the inhibition effect of the OCC-Li electrode on the growth of Li dendrites, the electrode microscopic morphology of the OCC-Li||OCC-Li and CC-Li||CC-Li symmetric cells at 1 mA cm^{-2}, 1 mA h cm^{-2} after 50 cycles is observed (Fig. 8). As observed in Fig. 8a–c, Li is uniformly distributed on the carbon fibre surface of the OCC-Li electrode

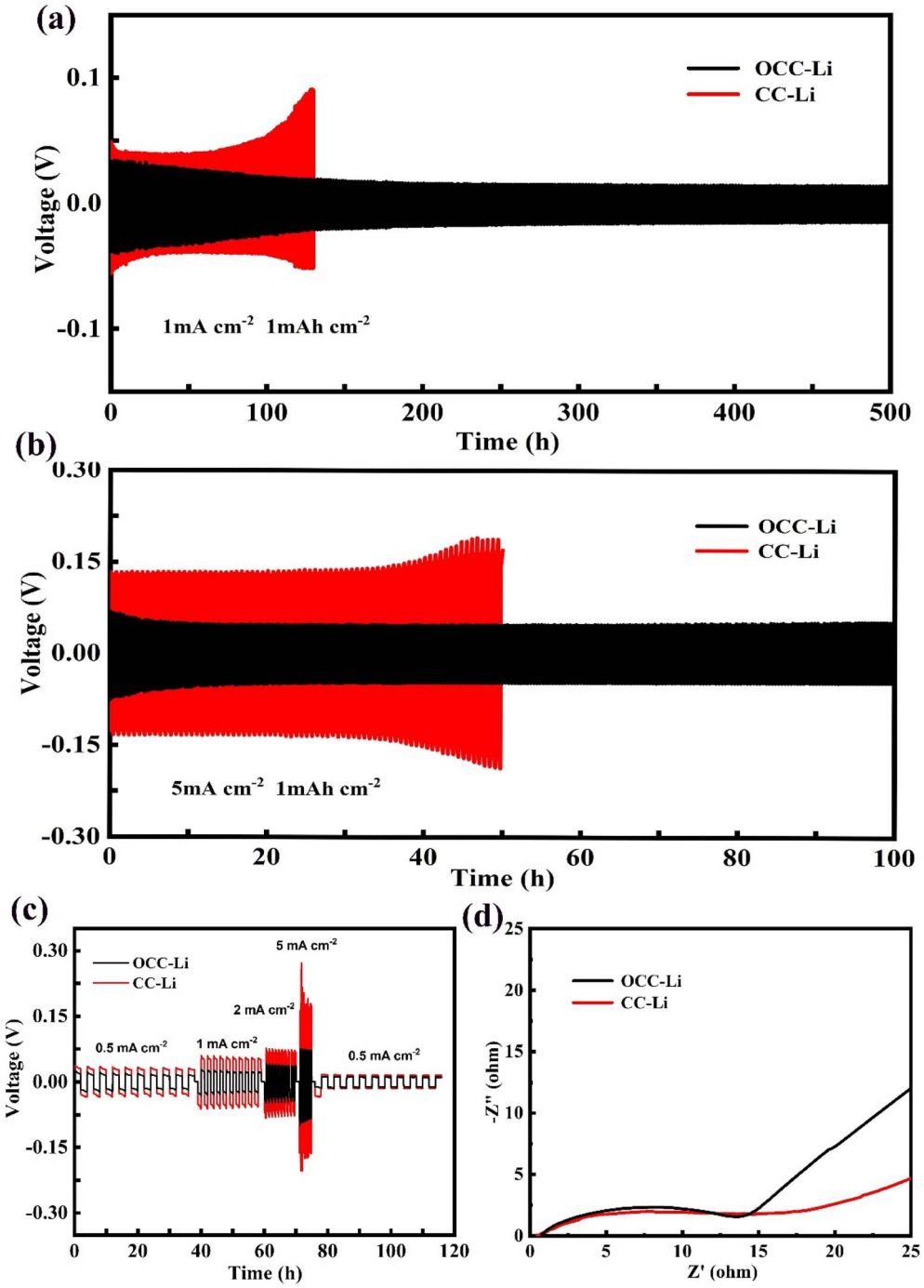

Fig. 7 The OCC-Li||OCC-Li and CC-Li||CC-Li symmetrical cells for 1 mA h cm^{-2} (a and b) voltage curves at 1 mA cm^{-2} and 5 mA cm^{-2}; (c) rate performance; (d) EIS Nyquist plots.

without the formation of dendritic and mossy Li and dead Li, suggesting that the lithophilic functional groups can induce the dense and uniform deposition of Li. In contrast, Li deposition on CC-Li electrodes is uneven and aggregation occurs due to its poor affinity, while the formation of dead Li results from the fracture of Li dendrites or the detachment of mossy Li from the substrate (Fig. 8d–f). In addition, to check the degree of Li consumption during the cycle, the XPS of OCC-Li and CC-Li composite electrodes after cycling are test (Fig. S7†). In the Li 1s of the OCC-Li and CCC-Li, the Li–O bond has a larger proportion, which indicates that the lipophilic oxygen-containing functional group in the OCC can adsorb Li^+ and effectively reduce the consumption of active Li.

To investigate the potential of the OCC-Li as a Li metal anode in practical applications, the OCC-Li||LFP full cells are assembled using LFP as the cathode, $LiPF_6$ as the electrolyte and the OCC-Li as the anode. Meanwhile, the CC-Li||LFP full cells are assembled for comparison. The load capacity of LFP is 9.3 mg

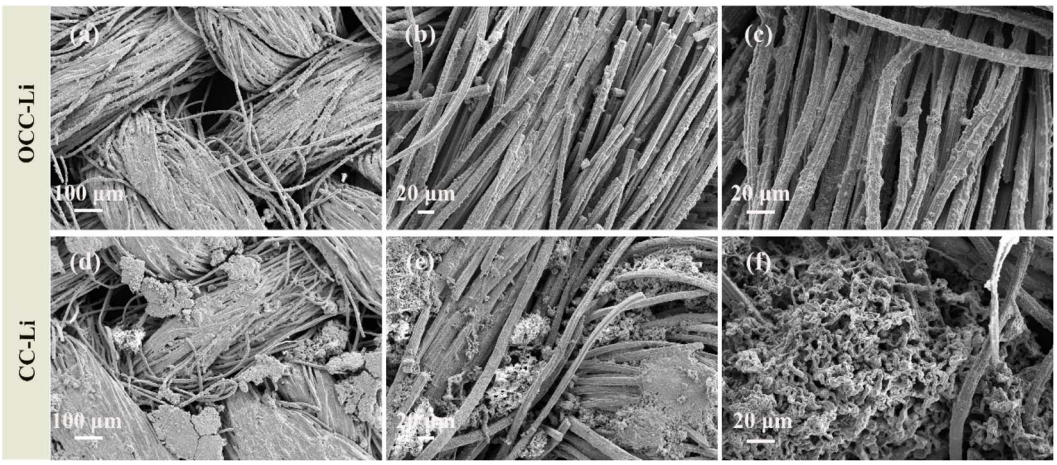

Fig. 8 Electrode morphology of symmetrical cells after 50 cycles at 1 mA cm^{-2}, 1 mA h cm^{-2} (a–c) OCC-Li and (d–f) CC-Li.

cm^{-2} (~1.60 mA h cm^{-2}) and the pre-deposited Li capacity of OCC-Li and CC-Li anodes are 3 mA h cm^{-2}. The long cycle performance of the full cells at 1C (1C = 172 mA g^{-1}) is demonstrated in Fig. 9a. The initial Coulomb efficiencies of OCC-Li||LFP and CC-Li||LFP full cells are 99.8% and 98.6%, respectively. The OCC-Li||LFP cell has a capacity of 117 mA h g^{-1} after 300 cycles, which maintains a high capacity retention rate (94.3%) and high CE (99.2%), attributed to the high interface stability and affinity of the OCC-Li electrode. In contrast, the capacity of the CC-Li||LFP cell is only 87 mA h g^{-1} after 50 cycles due to the inhomogeneous deposition of Li on the CC-Li and the excessive consumption of active Li during the cycle. Meanwhile,

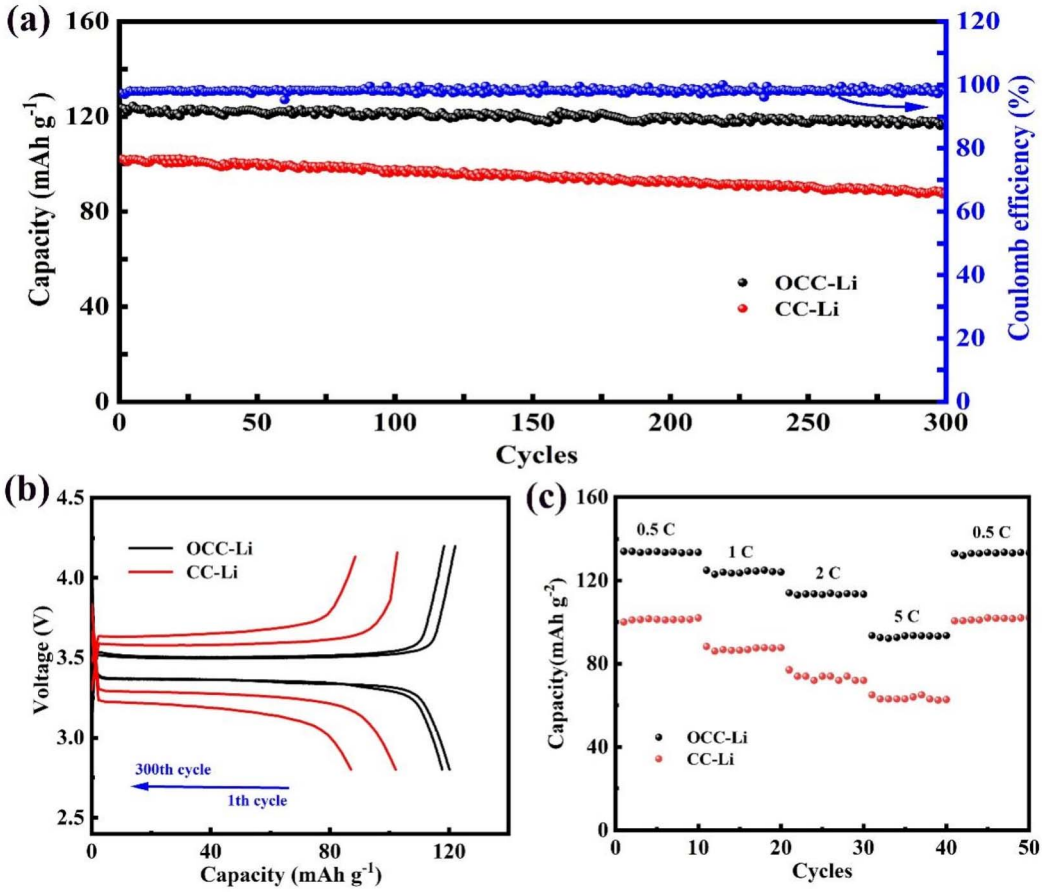

Fig. 9 Electrochemical performance of OCC-Li||LFP and CC-Li||LFP full cells (a) rate capability; (b) the voltage–capacity curves at 1C; (c) cyclic performance at 1C.

the capacity–voltage curves show that the polarisation voltage of the OCC-Li‖LFP is smaller than that of the CC-Li‖LFP at 1C, which proves that the former had stronger redox reaction kinetics. And the polarization voltage of CC-Li‖LFP cell increases obviously with the increase of the number of cycles and the rate, indicating that the Li^+ dynamics of CC-Li‖LFP cell becomes slow due to the rapid consumption of electrolyte (Fig. 9b and S8†). In addition, in Fig. 9c, the OCC-Li‖LFP cell shows superior rate performance (133.5, 124.5, 113.8, 93.4, and 132.7 mA h g^{-1}) than the OCC-Li‖LFP (101.5, 86.4, 74.1, 65.2, 101 mA h g^{-1}) at 0.5C, 1C, 2C, 5C and 0.5C. Therefore, the performance of the OCC-Li electrode in the full cells demonstrates its promising application.

4. Conclusions

In summary, the OCC as a collector for Li metal anode is prepared by a simple oxidation method and the deposition behaviour of Li in the OCC is investigated. The oxygen-containing functional groups (–COOH, –C–OH, C═O) enhance the lithophilicity of carbon fibres and lower the Li nucleation barrier. At the same time, the polar sites can regulate the dense and uniform deposition of Li^+, which avoids the formation of dendrites and the generation of dead Li. Consequently, the cross-sectional thickness variation of the OCC-Li electrode is smaller than that of CC-Li, indicating that OCC is effective in mitigating volume expansion. Moreover, the surface of OCC-Li electrode after cycling is compact and uniform without Li dendrite generation. On the electrochemical, the OCC‖Li exhibits stable Li deposition/exfoliation at 1 mA cm^{-2} after 250 cycles with high CE (99.1%). The OCC-Li‖OCC-Li symmetric cell is cycled stably for 500 h with a low polarisation voltage (15 mV). The OC-Li‖LFP full cell capacity is 117 mA h g^{-1} after 300 h cycle at 1C. The OCC-Li anode positively impacts the development of Li metal batteries with high energy density and long cycles.

Data availability

The data supporting this article have been included in the paper.

Conflicts of interest

The authors declare no conflict of interest.

Acknowledgements

This work was supported by the Science and Technology Plan Project of Qingyang (QY-STK-2022B-148, QY-STK-2024B-177). The authors would like to thank Shiyanjia Lab (https://www.shiyanjia.com) for the XPS test and Gansu Key Laboratory of Efficient Utilization of Oil and Gas Resources in Longdong.

References

1 Q. Lu, C. Liu, Y. Zhao, W. Pan, K. Xie, P. Yue, G. Zhang, A. Omar, L. Liu, M. Yu and D. Mikhailova, Freestanding mxene-based macroforms for electrochemical energy storage applications, *SusMat*, 2023, **3**, 471–497, DOI: 10.1002/sus2.151.

2 D. Wu and Z. Zhou, Recent progress of computational investigation on anode materials in Li ion batteries, *Front. Phys.*, 2011, **6**, 197–203, DOI: 10.1007/s11467-011-0186-z.

3 J. Liang, L. Zhang, D. XiLi and J. Kang, Research progress on tin-based anode materials for sodium ion batteries, *Rare Met.*, 2020, **39**, 1005–1018, DOI: 10.1007/s12598-020-01453-x.

4 N. Li, S. X. Jin, Q. Y. Liao and C. X. Wang, Zno anchored on vertically aligned graphene: binder-free anode materials for lithium-ion batteries, *ACS Appl. Mater. Interfaces*, 2014, **6**, 20590–20596, DOI: 10.1021/am507046k.

5 Y. Zhu, M. Ge, F. Ma, Q. Wang, P. Huang and C. Lai, Multifunctional electrolyte additives for better metal batteries, *Adv. Funct. Mater.*, 2024, **34**, 2301964, DOI: 10.1002/adfm.202301964.

6 J. Ding, Y. Zhang, R. Xu, R. Zhang, Y. Xiao, S. Zhang, C. Bi, C. Tang, R. Xiang, H. S. Park, Q. Zhang and J. Huang, Review on lithium metal anodes towards high energy density batteries, *Green Energy Environ.*, 2023, **8**, 1509–1530, DOI: 10.1016/j.gee.2022.08.002.

7 M. S. Kim, Z. Zhang, J. Wang, S. T. Oyakhire, S. C. Kim, Z. Yu, Y. Chen, D. T. Boyle, Y. Ye, Z. Huang, W. Zhang, R. Xu, P. Sayavong, S. F. Bent, J. Qin, Z. Bao and Y. Cui, Revealing the multifunctions of li_3n in the suspension electrolyte for lithium metal batteries, *ACS Nano*, 2023, **17**, 3168–3180, DOI: 10.1021/acsnano.2c12470.

8 J. Li, Y. Cai, H. Wu, Z. Yu, X. Yan, Q. Zhang, T. Z. Gao, K. Liu, X. Jia and Z. Bao, Polymers in Lithium-Ion and Lithium Metal Batteries, *Adv. Energy Mater.*, 2024, **25**, 2003239, DOI: 10.1002/aenm.202003239.

9 B. Wu, C. Chen, L. H. J. Raijmakers, J. Liu, D. L. Danilov, R. Eichel and P. H. L. Notten, Li-growth and sei engineering for anode-free li-metal rechargeable batteries: a review of current advances, *Energy Storage Mater.*, 2023, **57**, 508–539, DOI: 10.1016/j.ensm.2023.02.036.

10 T. Naren, G. C. Kuang, R. Jiang, P. Qing, H. Yang, J. Lin, Y. Chen, W. Wei, X. Ji and L. Chen, Reactive polymer as artificial solid electrolyte interface for stable lithium metal batteries, *Angew. Chem., Int. Ed.*, 2023, **62**, e202305287, DOI: 10.1002/anie.202305287.

11 K. Peng, P. Tang, Q. Yao, Q. Dou and X. Yan, Bifunctional fluoropyridinium-based cationic electrolyte additive for dendrite-free li metal anode, *Nano Res.*, 2023, **16**, 9530–9537, DOI: 10.1007/s12274-023-5761-4.

12 G. Liu, Y. Li, L. Zhang, H. Tao and X. Yang, In situ construction of high lithiophilic lithium phosphide protective layer for stable lithium metal anode, *Electrochim. Acta*, 2023, **471**, 143413, DOI: 10.1016/j.electacta.2023.143413.

13 J. Yang, H. L. Wan, Z. H. Zhang, G. Z. Liu, X. X. Xu, Y. S. Hu and X. Y. Yao, NASICON-structured $Na_{3.1}Zr_{1.95}Mg_{0.05}Si_2PO_{12}$ solid electrolyte for solid-state sodium batteries, *Rare Met*, 2018, **37**, 480–487, DOI: 10.1007/s12598-018-1020-3.

14 H. Kang, H. Kang, M. Lyu and E. Cho, A review of recent developments in the design of electrolytes and solid electrolyte interphase for lithium metal batteries, *EcoMat*, 2024, **6**, e12498, DOI: 10.1002/eom2.12498.

15 Z. Hao, Y. Lu, G. Yang, Q. Zhao, Z. Yan and J. Chen, Designing current collectors to stabilize Li metal anodes, *Adv. Mater.*, 2025, **37**, 2415258, DOI: 10.1002/adma.202415258.

16 H. Dou, Z. Zhao, S. Yang, X. Wang and X. Yang, The role of carbon materials in suppressing dendrite formation in lithium metal batteries, *New Carbon Mater.*, 2023, **38**, 599–618, DOI: 10.1016/S1872-5805(23)60762-0.

17 Q. Yun, Y. B. He, W. Lv, Y. Zhao, B. Li, F. Kang and Q. H. Yang, Chemical dealloying derived 3d porous current collector for Li metal anodes, *Adv. Mater.*, 2016, **28**, 6932–6939, DOI: 10.1002/adma.201601409.

18 L. Chen, H. Liu, M. Li, S. Zhou, F. Mo, S. Yu and J. Wei, Boosting the performance of lithium metal anodes with three-dimensional lithium hosts: recent progress and future perspectives, *Batteries*, 2023, **9**, 391, DOI: 10.3390/batteries9080391.

19 G. Luo, X. Yin, D. Liu, A. Hussain, F. Liu and X. Cai, Electrosynthesis of vertically aligned zinc oxide nanoflakes on 3D porous cu foam enables dendrite-free li-metal anode, *ACS Appl. Mater. Interfaces*, 2022, **14**, 33400–33409, DOI: 10.1021/acsami.2c09287.

20 L. You, J. Liu, H. Zhang, T. Zhang, J. Wang, Z. Guo, G. Xia and X. Yu, Building a house for stabilizing lithium-metal anodes, *Batteries Supercaps*, 2022, **5**, e202100408, DOI: 10.1002/batt.202100408.

21 D. Wang, H. Liu, F. Liu, G. Ma, J. Yang, X. Gu, M. Zhou and Z. Chen, Phase-separation-induced porous lithiophilic polymer coating for high-efficiency lithium metal batteries, *Nano Lett.*, 2021, **21**, 4757–4764, DOI: 10.1021/acs.nanolett.1c01241.

22 X. Sun, J. Man, K. Liu, W. Liu, J. Sun, N. Zhang, Y. Zhou, Z. Geng, S. Li and J. Sun, Uniform lithium deposition enabled by a carbon nanotubes framework modified with nanosized ZIF-8 particles for dendrite-free lithium metal anode, *Appl. Surf. Sci.*, 2023, **616**, 156474, DOI: 10.1016/j.apsusc.2023.156474.

23 Z. Zhuang, X. Rao, F. Zhang, V. V. Jadhav and D. Q. Tan, Plasma-activated tightly bonded uniform metal-organic framework on carbon cloth for stable Li metal anode, *J. Power Sources*, 2024, **605**, 234540, DOI: 10.1016/j.jpowsour.2024.234540.

24 J. Zhang, Z. Su, J. Jin, S. Yang, A. Yu and G. Li, High-coulombic-efficiency lithium metal anodes enabled by three-dimensional lithiophilic nanostructures with multiscale porosity, *ACS Sustainable Chem. Eng.*, 2022, **10**, 13629–13637, DOI: 10.1021/acssuschemeng.2c03271.

25 Z. Du, J. Bi, Z. Zhou, Y. Liu, L. Xing and W. Ai, Deformation-adaptive n,p-doped porous carbon nanofibers as a protective interlayer for stable li metal anodes, *Acta Mater.*, 2025, **283**, 120584, DOI: 10.1016/j.actamat.2024.120584.

26 Y. Tian, Z. Pei, D. Luan and X. W. D. Lou, Anchoring sn nanoparticles in necklace-like b,n,f-doped carbon fibers enables anode-less 5v-class Li-metal batteries, *Angew. Chem., Int. Ed.*, 2025, **64**, e202423454, DOI: 10.1002/anie.202423454.

27 K. Baek, W. Lee, E. Im, J. H. Ha, S. Ahn, Y. Kim, Y. Choi and S. J. Kang, Gradient lithium metal infusion in Ag-decorated carbon fibers for high-capacity lithium metal battery anodes, *Nano Lett.*, 2023, **23**, 8515–8523, DOI: 10.1021/acs.nanolett.3c02229.

28 L. Zhou, H. Yuan, R. Fang, H. Huang, Y. Gan, Y. Xia, J. Zhang, X. Xia, X. He and W. Zhang, A stable lithium metal anode enabled by the site-directed lithium deposition of ZnO-nanosheet-modified carbon cloth, *ChemSusChem*, 2024, **17**, e202400159, DOI: 10.1002/cssc.202400159.

29 X. Fan, Y. Li, C. Luo, S. Luo, B. Huang, S. Liu and W. Sun, Vertically aligned MnO_2 nanosheets on carbon fiber cloth as lithiophilic host enables dendrite-free lithium metal anode, *Electrochim. Acta*, 2023, **464**, 142896, DOI: 10.1016/j.electacta.2023.142896.

30 M. Liu, J. Ma, X. Zhang, J. Wang, Y. Fan, A. Song, G. Shao and Z. Ma, Regulating of lithium-ion dynamic trajectory by ferromagnetic CoF_2 to achieve ultra-stable deep lithium deposition over 10000 h, *Adv. Funct. Mater.*, 2024, **35**, 2416527, DOI: 10.1002/adfm.202416527.

31 N. Zhu, Y. Yang, Y. Li, Y. Bai, J. Rong and C. Wu, Carbon-based interface engineering and architecture design for high-performance lithium metal anodes, *Carbon Energy*, 2024, **6**, e423, DOI: 10.1002/cey2.423.

32 Y. Ren, S. Chen, M. Odziomek, J. Guo, P. Xu, H. Xie, Z. Tian, M. Antonietti and T. Liu, Mixing Functionality in Polymer Electrolytes: A New Horizon for Achieving High-Performance All-Solid-State Lithium Metal Batteries, *Angew. Chem., Int. Ed.*, 2025, e202422169, DOI: 10.1002/anie.202422169.

33 Y. Feng and H. Liu, From non-carbon host toward carbon-free lithium-sulfur batteries, *Nano Res.*, 2024, **17**, 1337–1365, DOI: 10.1007/s12274-023-5945-y.